Journal of Power Sources 273 (2015) 793–803

Contents lists available at ScienceDirect

Journal of Power Sources

journal homepage: www.elsevier.com/locate/jpowsour

Combined State of Charge and State of Health estimation over lithium-ion battery cell cycle lifespan for electric vehicles

Yuan Zou [a, *], Xiaosong Hu [b], Hongmin Ma [a], Shengbo Eben Li [c]

[a] National Engineering Lab for Electric Vehicles, School of Mechanical Engineering, Beijing Institute of Technology, No. 5 Zhongguancun South Street, Haidian District, Beijing 100081, China
[b] Energy, Controls, and Applications Lab, University of California, Berkeley, CA 94720, USA
[c] State Key Lab of Automotive Safety and Energy, Dept. of Automotive Eng., Tsinghua University, Beijing 100084, China

HIGHLIGHTS

- Performance degradation of lithium-ion battery over the cell lifetime is quantified.
- State estimators with the different time scales are developed for SOC and SOH identification.
- Capacity fade and power fade are accurately characterized.
- SOC estimator is accurate and robust over the life span of the battery cell.

ARTICLE INFO

Article history:
Received 16 March 2014
Received in revised form
18 September 2014
Accepted 22 September 2014
Available online 2 October 2014

Keywords:
Electric vehicles
Lithium-ion battery
Kalman filter
Recursive least squares
State of charge
State of health

ABSTRACT

A combined SOC (State Of Charge) and SOH (State Of Health) estimation method over the lifespan of a lithium-ion battery is proposed. First, the SOC dependency of the nominal parameters of a first-order RC (resistor-capacitor) model is determined, and the performance degradation of the nominal model over the battery lifetime is quantified. Second, two Extended Kalman Filters with different time scales are used for combined SOC/SOH monitoring: the SOC is estimated in real-time, and the SOH (the capacity and internal ohmic resistance) is updated offline. The time scale of the SOH estimator is determined based on model accuracy deterioration. The SOC and SOH estimation results are demonstrated by using large amounts of testing data over the battery lifetime.

1. Introduction

Lithium-ion batteries have been widely used in modern electrified vehicles. The reliable, efficient, and safe operation of lithium-ion batteries requires monitoring, control and management. For battery management systems, a core function is to provide accurate estimates of State of Charge (SOC) and State of Health (SOH) of batteries, which is challenging due to the lack of sensors for electrochemical phenomena inside the cells.

Many methods were proposed to estimate the battery SOC, each with its own advantages and disadvantages, as summarized in Table 1. The Coulomb counting method and open circuit voltage method are widely used in battery management systems of electrified vehicles. They are easy to use and fast in computation, but the former highly relies on the performance of current sensor, and the latter is not effective for batteries with flat open-circuit-voltage curve. Another disadvantage for Coulomb counting is that this method is open-loop estimation and may have large accumulated error due to uncertainties or disturbances [1–5]. Moreover, it requires accurate initial SOC value. Many artificial intelligence-based methods have been applied to establish black-box SOC estimation models, such as neural network [6], fuzzy logic [7], and support vector regression (SVR) models [8]. The Kalman filter (KF) and sliding mode observer have also been used to predict the battery SOC. These approaches are model-based, closed-loop, and thus can use output feedback to keep better robustness than non-feedback methods. In Refs. [9–11], the extended Kalman filter (EKF) concept, based on nonlinear state-space models, was used to

* Corresponding author. Tel./fax: +86 10 6891 8837.
E-mail addresses: zouyuan@bit.edu.cn, zouyuan05@gmail.com (Y. Zou).

http://dx.doi.org/10.1016/j.jpowsour.2014.09.146
0378-7753/

Table 1
Advantages and disadvantages of existing SOC and SOH estimation methods.

State of charge (SOC)			State of health (SOH)			
Method	Advantage	Disadvantage	Method		Advantage	Disadvantage
Coulomb counting [1–4]	Simple	Open-loop, sensitive to the current sensor precision, and uncertain to initial SOC	Durability model-based open-loop method	Durability mechanism [23,24]	Comprehensive understanding	Complex, need accurate input parameters
Open circuit voltage method [5]	Simple	Open-loop, sensitive to the voltage sensor precision, unsuitable for cells with flat OCV–SOC curves		Durability external characteristic [25–28]	Simple and easy to predict capacity fade and internal resistance increment	Based on a large number of experiments
Neural network [6]	Generic, good nonlinearity mapping approximation	Sensitive to the amount and quality of training data	Battery model-based parameter identification closed-loop method	DC resistance [21]	Simple	Not accuracy, sensitive to disturbances
Fuzzy logic [7]	Generic, good nonlinearity mapping approximation	Sensitive to the amount and quality of training data		AC impedance [22]	Accuracy	Complex
Support vector machine [8]	Generic, good nonlinearity mapping	Sensitive to the amount and quality of training data		Extend Kalman filter [11,29]	Quite easy to implement, accurate	Sensitive to modeling accuracy
Kalman filter [9–18]	Closed-loop, online, accuracy	More computationally expensive than non-feedback methods, and highly depend on the model accuracy.		Fuzzy logic [30]	Accuracy simple, accurate	Slow convergence
				Sample entropy [31–33]	Simple	Need large amount of data
Sliding mode observer [19,20]	Closed-loop, online, and accurate	More computationally expensive than non-feedback methods, and highly depend on the model accuracy.		Discharge voltage [30]	Easy	Not accurate
				Adaptive control system [31]	Online	Sensitive to modeling accuracy

estimate the SOC of a Li-polymer battery. Several other variants of Kalman filter, e.g. sigma-point KF [12,13], adaptive KF [14–16], Dual KF [17] and derivative KF [18] have also been used for battery SOC estimation. The sliding-mode observer technique has also been used to monitor battery SOC trajectories [19,20].

State of Health (SOH) is a metric to evaluate the aging level of batteries, which often includes capacity fade and/or power fade. The commonly used indicators include battery capacity [11], DC resistance [21], and AC impedance [22]. The SOH estimation methods mainly include durability model-based open-loop methods and battery model-based closed-loop method [5]. The former methods directly predict the changes in capacity fade and internal resistance. The durability models describe the increase of SEI film resistance and battery terminal voltage [23,24]. Based on durability characteristics, a storage life model for lithium cobalt oxides batteries was given in Ref. [25]. Bloom et al. [26] obtained the relationship between the battery performance degradation and ambient temperatures and cycle time. Matsushima [27] also found that capacity loss exhibits a square root relationship with time. Li et al. [28] developed an extended Arrhenius model. The battery model-based closed-loop methods use least-squares methods, Kalman filtering [29] and other adaptive algorithms (such as fuzzy logic [30]), to identify the battery capacity and internal resistance according to the operating data. Sample Entropy was also used to estimate the battery SOH in Refs. [31–33]. The advantages and disadvantages of these SOH methods are summarized in Table 1.

Most of the above mentioned battery-state-estimation methods were developed for either SOC or SOH estimation, and not both. The intimate coupling feature between SOC and SOH was overlooked. The accuracy of SOC estimation is heavily influenced by battery degradation. As batteries degrade, SOC-only estimation algorithms may lead to large errors. The inaccurate SOC estimations in turn may mislead the battery SOH calibration. Therefore, simultaneous estimation of SOC and SOH is quite beneficial. Compared to the battery SOC variation, battery SOH typically change much more slowly, necessitating multi-timescale state estimators. In order to determine the appropriate time scale for the SOH estimator, it is critical to examine the performance degradation of the battery model in the context of battery aging. The multi-scale EKFs are used to estimate SOC and SOH, and the capacity estimation is periodically introduced in SOC update equation [34,35]. It is more computational efficient than a joint estimation [34]. However, the determination of the two time scales is heavily dependent on the tuition and calibration.

This paper discusses a model-based combined SOC/SOH estimation method over the lifespan of LiNMC batteries. First, the SOC dependence of the nominal parameters of a first-order RC (resistor–capacitor) model is determined, and the performance degradation of the nominal model is quantified over the battery lifetime. Second, two EKFs with different time scales are applied to implement the combined SOC/SOH monitoring: one observer is for real-time SOC estimation; the other for offline SOH (capacity and internal resistance) update. The time scale of the SOH estimator is determined based on the quantified model accuracy degradation. The SOC and SOH estimation results are demonstrated by using large amounts of testing data over the battery lifetime.

The remainder of the paper is arranged as follows: Section 2 introduces the battery model structure and battery tests; the degradation of a nominal battery model is described in Section 3; the combined SOC/SOH estimation approach and associated results are discussed in Section 4; Section 5 concludes this paper.

2. Battery modeling

2.1. Equivalent circuit model

Hu et al. [36] compared 12 commonly used equivalent circuit models and concluded that the first-order RC model is the best choice considering model complexity, accuracy, and robustness. Fig. 1 shows the model structure considered. The battery capacity C_{cap} is used to quantify SOC level by Eq. (1)

$$\dot{SOC} = -\frac{\eta \cdot I_{batt}}{3600 \cdot C_{cap}} \tag{1}$$

The Coulombic efficiency η is simplified as the constant value, 1.0 during the discharge and 0.98 in charging.

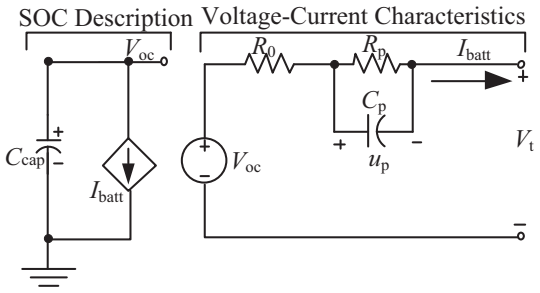

Fig. 1. Battery model structure: open circuit voltage V_{oc}, series resistance R_0, diffusion resistance R_p, and diffusion capacitance C_p; current I_{batt}, terminal voltage V_t, and battery capacity C_{cap}.

The capacity calibration is carried out by Constant Current Constant Voltage (CCCV) reference test. Controlled current source I_{batt} representing the current flow in the cell, acts as the input variable. Controlled voltage source V_{oc} stands for the cell Open Circuit Voltage (OCV). Terminal Voltage V_t is the output variable. The ohmic resistance R_0 describes the internal ohmic resistance. The mathematical equations are shown below:

$$\begin{cases} \dot{u}_p = -\dfrac{u_p}{C_p R_p} + \dfrac{I_{batt}}{C_p} \\ V_t = V_{oc} - u_p - I_{batt} R_0 \end{cases} \tag{2}$$

where u_p is the voltage across the parallel RC network.

2.2. Battery testing systems and schedule

The test data used for this study were acquired through the battery testing facility in Refs. [33,36]. The data acquisition frequency is 10 Hz. The batteries used for this test are lithium nickel–manganese–cobalt (LiNMC) UR14650P cells from Sanyo with a graphite anode. Its main specifications are listed in Table 2. Eight cells were tested with the compound load profiles for comparison and validation. As shown in Fig. 2, the experiment procedure starts with a series of characterization tests at three different temperatures (in the order of 10 °C, 35 °C and 22 °C). Each characterization test consists of a static capacity test using current rate 0.5C, a hybrid pulse test, a DC resistance test, a dynamic stress test (DST), and a Federal Urban Driving Schedule (FUDS) test. After these tests, aging cycles are conducted at 22 °C. In each aging cycle, the cells are charged and discharged at a constant rate until the cut-off voltage is reached. More detailed discussion of the battery testing systems and schedules can be found in Ref. [36].

Table 2
Main specifications of the LiNMC cell.

Nominal capacity (Ah)	Nominal voltage (V)	Upper cut-off voltage (V)	Lower cut-off voltage (V)
0.94	3.70	4.20	2.50

3. Battery model parameter identification

3.1. Identification method

Fig. 3 shows the data collected in the hybrid pulse test at 22 °C, and Fig. 4 is a magnified view of one discharge pulse at around 90% SOC. The detailed procedure is illustrated as follows:

(1) The V_{oc} value is determined from the steady-state voltage, as shown in Fig. 4(b).
(2) The ohmic resistance R_0 is proportional to the instantaneous voltage drop dV following a discharge pulse.

$$R_0 = \frac{dV}{i_0} \tag{3}$$

(3) The polarization resistance and capacitance (R_p, C_p) are related to the voltage amplitude change following the instantaneous potential variation described above, as shown in Fig. 4(b). The Recursive Least Squares (RLS) algorithm is used for (R_p, C_p) extraction. The linear identifiable form is derived by

$$\begin{cases} V(k) - V_{oc}(k) + V_{oc}(k-1) - V(k-1) = a_1 I(k) + a_2 I(k-1) \\ a_1 = \dfrac{-R_p C_p R_0 - (R_p + R_0)\Delta t}{\Delta t} \\ a_2 = \dfrac{R_p C_p R_0}{\Delta t} \end{cases} \tag{4}$$

where a_1 and a_2 are two parameters to be identified by RLS, given V_{oc} and R_0 from the above two steps. The associated RLS parameterization is described by

$$\begin{cases} \boldsymbol{G}(k) = \dfrac{\boldsymbol{P}(k-1)\boldsymbol{\varphi}(k)}{1 + \boldsymbol{\varphi}^T(k)\boldsymbol{P}(k-1)\boldsymbol{\varphi}(k)}, \\ \boldsymbol{\theta}(k) = \boldsymbol{\theta}(k-1) + \boldsymbol{G}(k)\left[V(k) - V_{oc}(k) + V_{oc}(k-1) - V(k-1) - \boldsymbol{\varphi}^T(k)\boldsymbol{\theta}(k-1)\right], \\ \boldsymbol{P}(k) = \boldsymbol{P}(k-1) - \boldsymbol{G}(k)\boldsymbol{\varphi}^T(k)\boldsymbol{P}(k-1), \end{cases} \tag{5}$$

where

$$\begin{cases} \boldsymbol{\varphi}(k) = [I(k), I(k-1)]^T, \\ \boldsymbol{\theta}(k) = [a_1, a_2]^T. \end{cases} \tag{6}$$

The initial values of the parameter estimate $\boldsymbol{\theta}(0)$ and its error covariance matrix $\boldsymbol{P}(0)$ need to be firstly prescribed. After calibrating $\boldsymbol{\theta}$, R_p and C_p can be easily determined by Eq. (4). The standard RLS algorithm and some variants were often used for battery modeling [37,38].

(4) Assuming that the initial voltage across the RC network u_p is equal to zero, due to the zero state response of RC circuit, the dynamics of u_p is

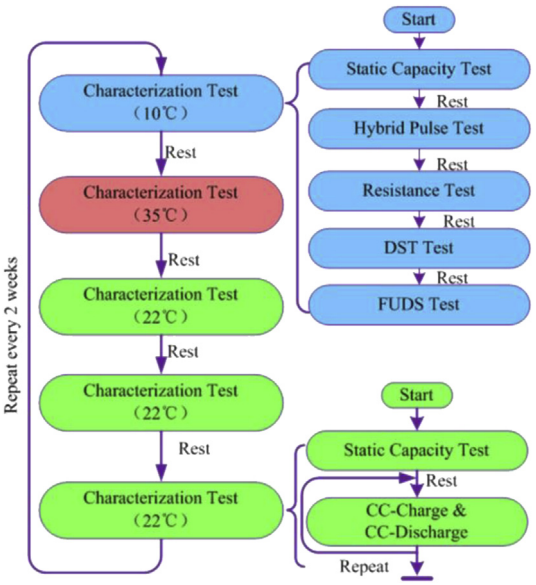

Fig. 2. Battery test schedule.

$$\begin{cases} u_p(k+1) = e^{-\Delta t/\tau}u_p(k) + I_{batt}R_p(1-e^{-\Delta t/\tau}) \\ \tau = R_pC_p \\ u_p(0) = 0 \end{cases} \quad (7)$$

where k is the time step. The above procedure at different SOC values is repeated to establish the SOC dependency of the model parameters.

3.2. Battery parameter estimation result

The modeling results include the following:

(1) The V_{oc}–SOC curve indicated in Fig. 5(a) is fitted by a sixth-order polynomial with 95% confidence bounds and a RMSE of 0.008328.
(2) The relationship between R_0 and SOC in Fig. 5(b) is fitted using a quadratic polynomial with 95% confidence bounds and a RMSE of 0.0008608.
(3) As shown in Fig. 5(c) and (d), the parameters of the RC network (R_p, C_p) as a function of SOC are approximated by exponential functions. The τ is the time constant of RC network.

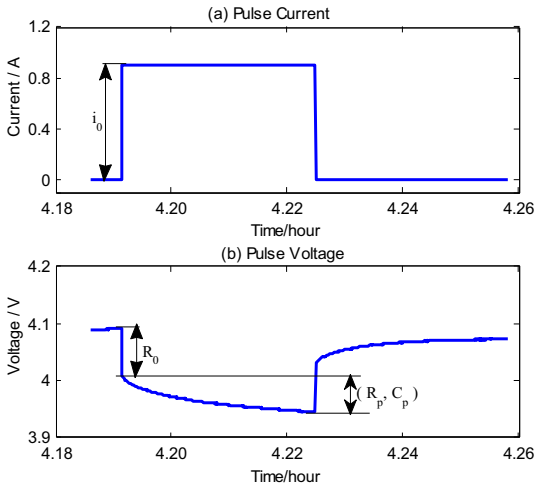

Fig. 4. Zoom-in (120 s) discharge pulse of the LiNMC cell at round 90% SOC at 22 °C.

3.3. Parameters estimation result discussion

The model identified was built in Simulink environment, and the evaluation result in the hybrid pulse test is shown in Fig. 6. There is good agreement between the model and the experimental data in the training dataset at 22 °C (i.e., hybrid pulse test), and the maximum relative error is less than 1.5%.

A series of "unseen" tests were conducted to verify and validate the model. The robustness of the model is validated based on different dynamic loading profiles at 22 °C, as shown in Figs. 7 and 8. The mean relative errors are 0.1617% and 0.144% in the DST and FUDS tests, respectively. The maximum relative errors in both tests are less than 1%.

Fig. 9 shows the errors of the nominal model at different cell aging levels under 22 °C. It indicates that as the aging number N increases, the mean and maximum errors of the nominal model increase. Based on the quantitative analysis, the model parameters are to be updated when a significant deviation from the measured cell voltage is detected. Possible trigger variable to identify a loss in model accuracy is the instantaneous voltage difference from the measured value, or the average voltage error over a drive cycle. The actual trigger threshold can be context specific and relevant to the particular criteria of the target application.

Based on Fig. 9, an average relative model error of 0.7% is here chosen as the trigger threshold, which is quite useful to design the time scale of the subsequent SOH estimator.

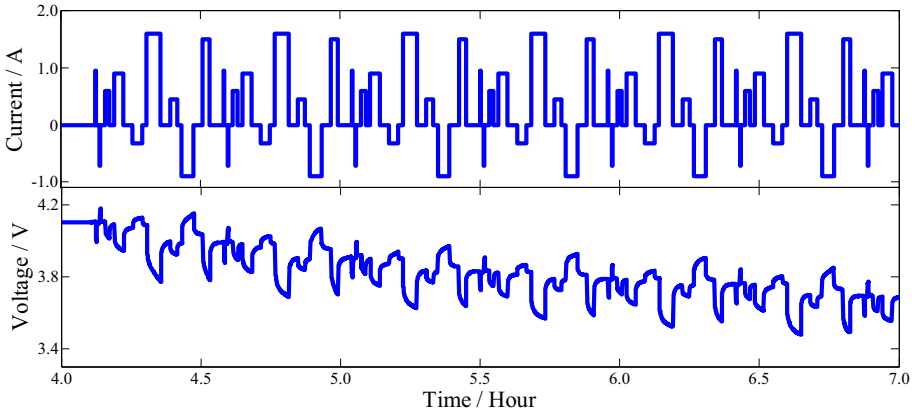

Fig. 3. Current, voltage, and SOC of the LiNMC cell in the training dataset at 22 °C.

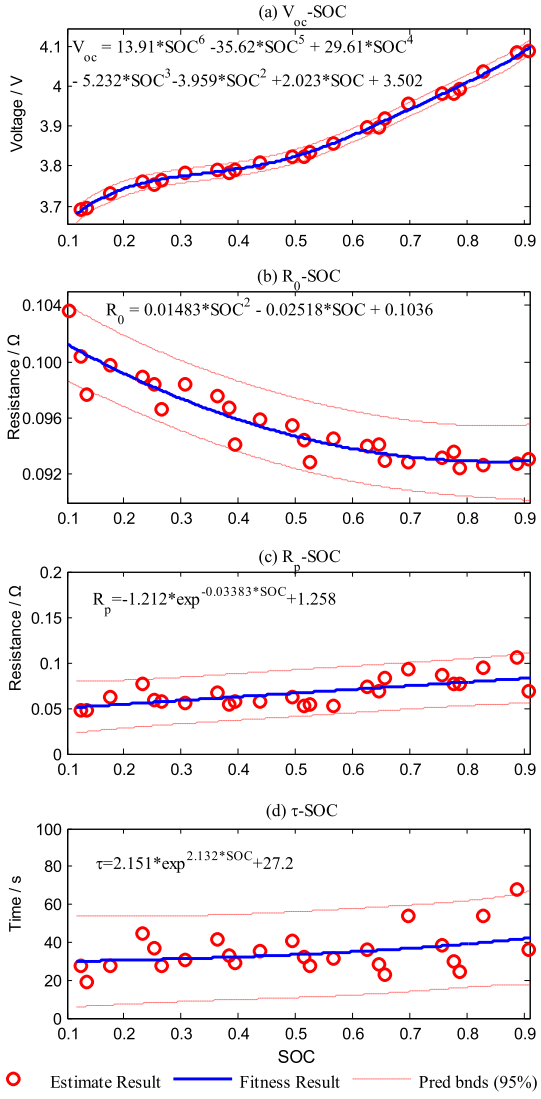

Fig. 5. Parameter estimation result in HPPC at 22 °C.

4. Combined SOC and SOH estimation

The increasing estimation error results from the variations of model parameters as the battery cell ages. To keep the sufficient accuracy of SOC estimation, it is plausible to update the parameters through the combined estimation of SOC and SOH, whenever the error of SOC estimation is unacceptable. Fig. 10 shows the multi-scale state estimation framework. By offline checking the accuracy decline of the nominal model, we can determine whether it is time to update the parameters (i.e., to trigger the SOH estimator). For offline parameters recalibration and SOH estimation, a fourth-order EKF is used. The state vector is

$$\mathbf{x} = \begin{bmatrix} \mathrm{SOC} & u_p & R_0 & 1/C_{cap} \end{bmatrix}^T.$$

The state space function is indicated below,

$$\begin{aligned} \mathbf{x}(k+1) &= \mathbf{A}(k)\mathbf{x}(k) + \mathbf{B}(k)I(k) \\ \mathbf{y}(k+1) &= \mathbf{C}(k)\mathbf{x}(k) \end{aligned} \tag{8}$$

where

$$\mathbf{A}(k) = \begin{pmatrix} 1 & 0 & 0 & -\dfrac{\eta \cdot \Delta t \cdot I(k)}{3600} \\ 0 & e^{-\frac{\Delta t}{R_p \cdot C_p}} & 0 & 0 \\ 0 & 0 & 1 & 0 \\ 0 & 0 & 0 & 1 \end{pmatrix}$$

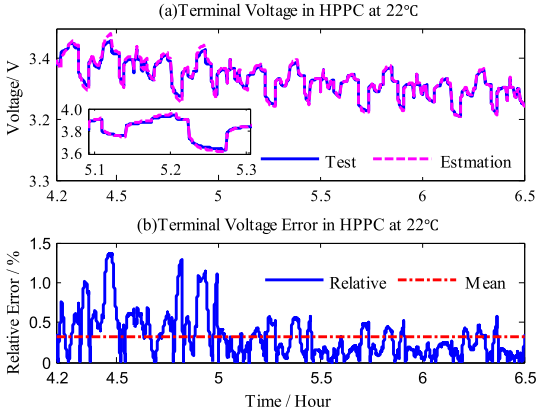

Fig. 6. Validation result in the hybrid pulse test at 22 °C.

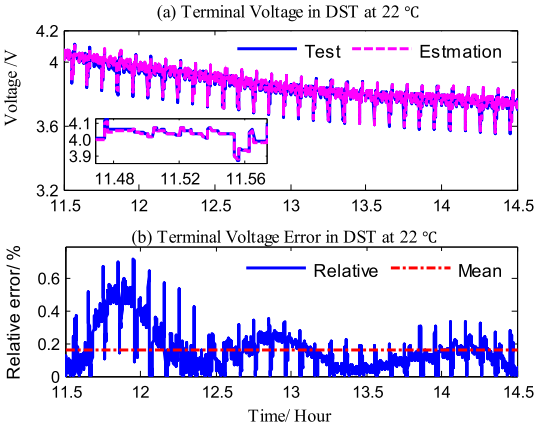

Fig. 7. Validation result in the DST test at 22 °C.

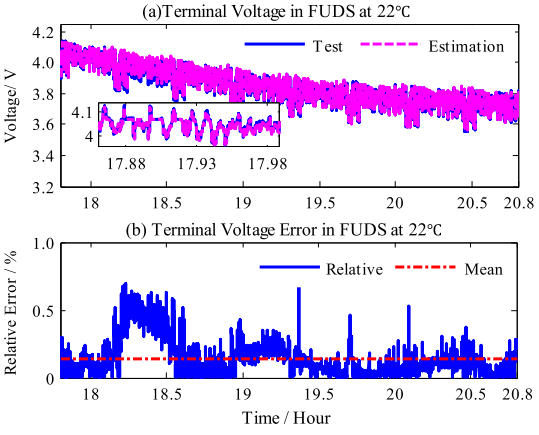

Fig. 8. Validation result in the FUDS test at 22 °C.

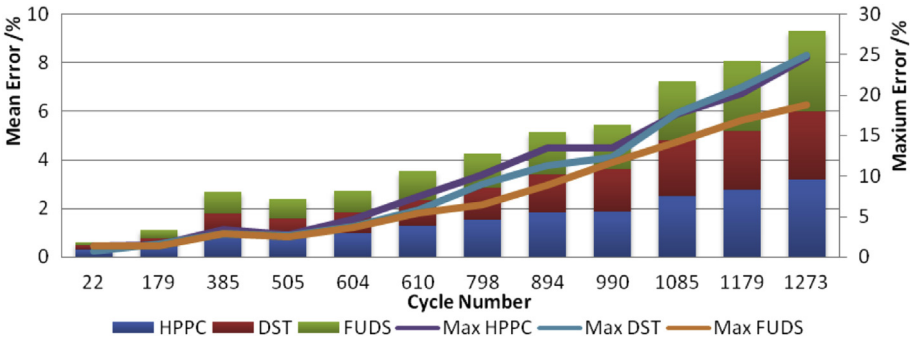

Fig. 9. Mean and maximum relative errors of the nominal model at different battery health levels.

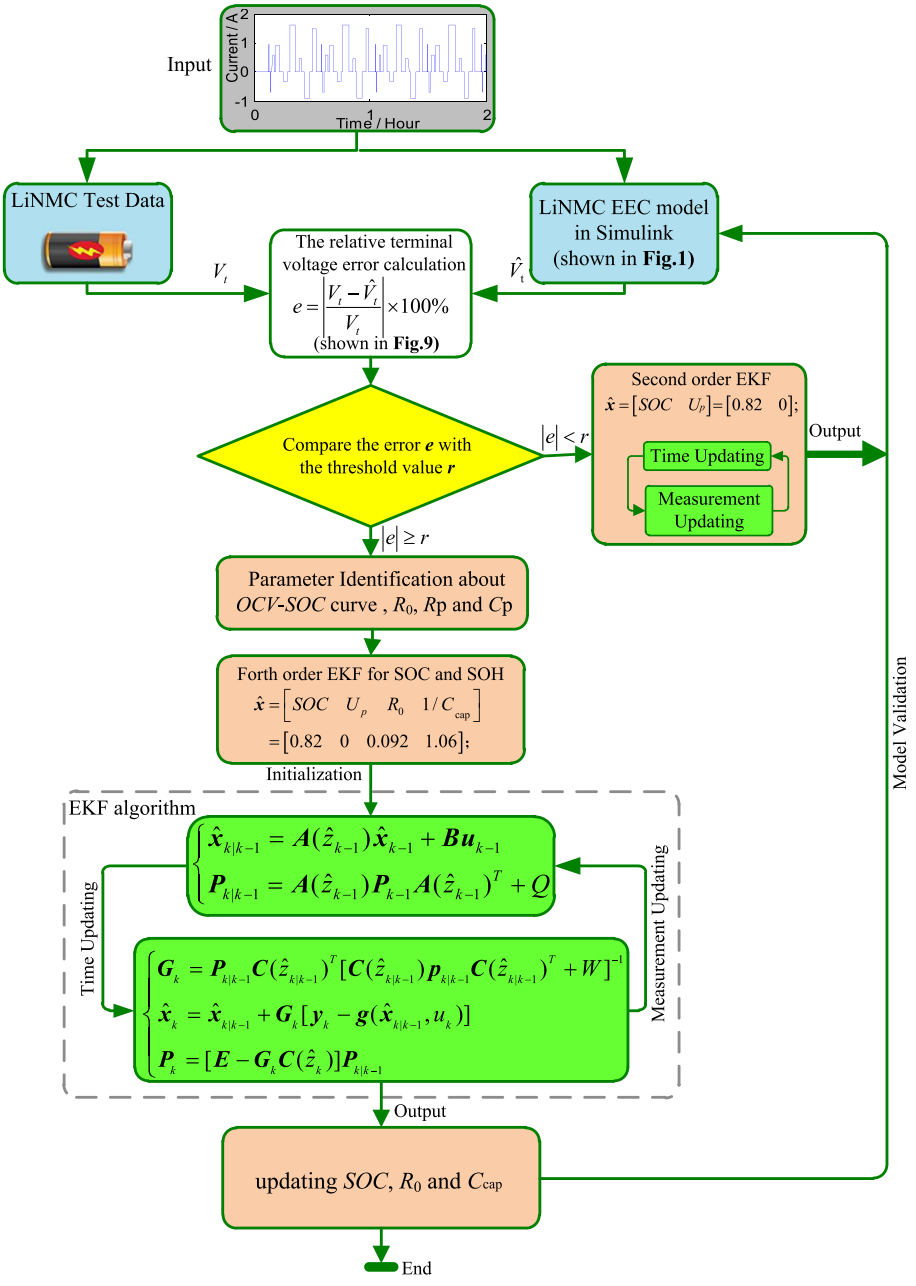

Fig. 10. Schematic of the combined SOC/SOH estimation.

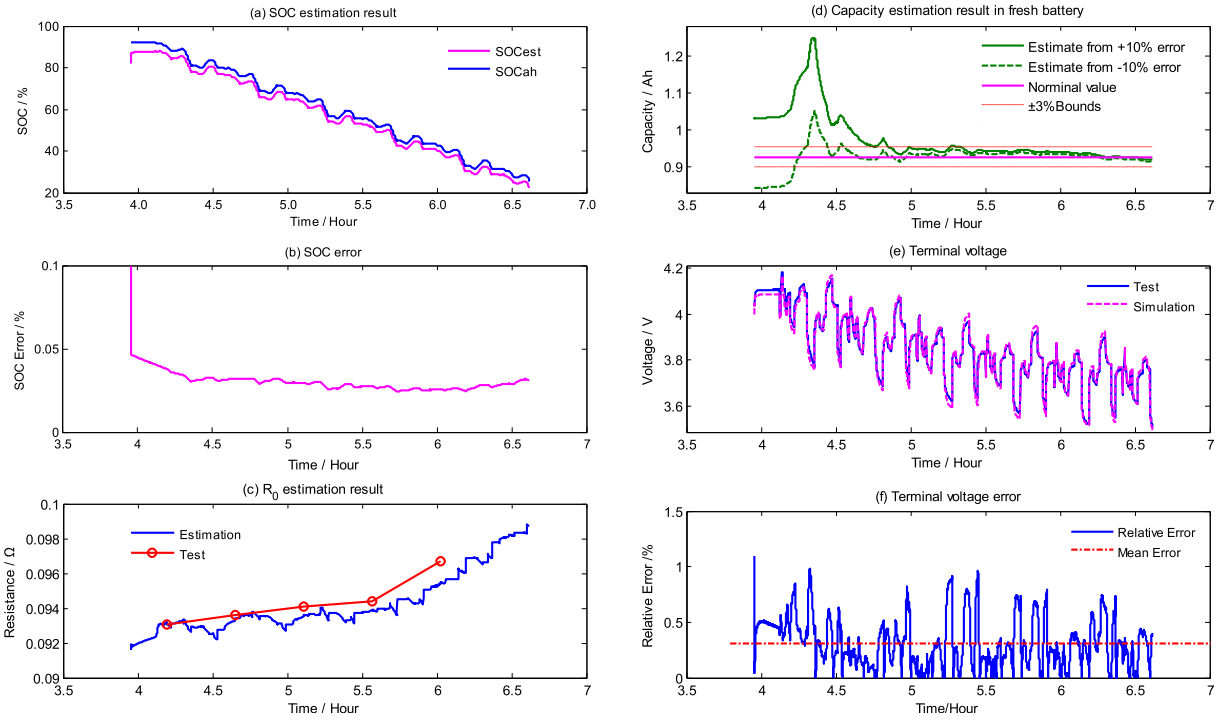

Fig. 11. State estimation result during the hybrid pulse test in the cycle 22 at 22 °C.

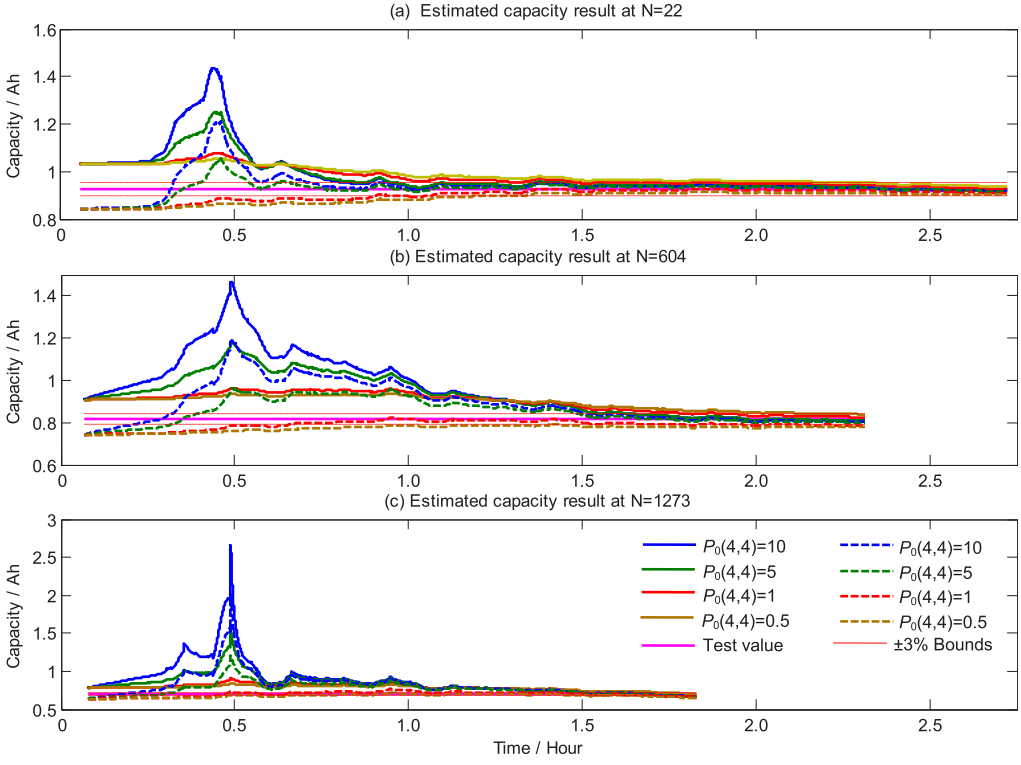

Fig. 12. Capacity estimation with different EKF initial parameters and cycle numbers during the hybrid pulse test at 22 °C.

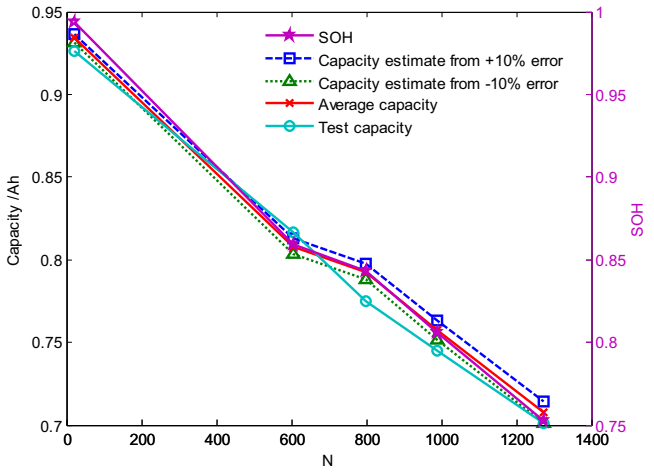

Fig. 13. Capacity and SOH estimation.

$$\mathbf{B}(k) = \begin{pmatrix} 0 \\ R_p \cdot \left(1 - e^{-\frac{\Delta t}{R_p \cdot C_p}}\right) \\ 0 \\ 0 \end{pmatrix}$$

$$\mathbf{C}(k) = \begin{pmatrix} \frac{df}{dx_1} & -1 & -I(k) & 0 \end{pmatrix}$$

$$f(\mathrm{SOC}) = a_1 \cdot \mathrm{SOC}^6 + a_2 \cdot \mathrm{SOC}^5 + \ldots a_6 \cdot \mathrm{SOC} + a_7.$$

where Δt is sample time, 0.1 s. Here, $f(\mathrm{SOC})$ is the fitted polynomial of OCV–SOC relation. EKF algorithm equations are not elaborated in the text but shown in Fig. 10. As introduced in Section 3, the average relative error threshold r is 0.7%.

Fig. 11 shows the estimation results from the fourth EKF for the fresh battery during the hybrid pulse test in the cycle 22 at 22 °C. The SOC estimation error is less than 0.1% during the most of the time, and the estimated resistance is closed to the test value. The estimated capacity converges toward the calibrated value reasonably whenever the initial guess starts from the values with ±10% relative error. The estimated terminal voltage almost superposes the test value, and the mean error is less than 0.5%.

Fig. 12 highlights that the capacity estimation converges toward the test value when the battery degrades at the different levels whenever the battery is almost new ($N = 22$), served for a while ($N = 604$) or used heavily ($N = 1273$). It should be noted that the estimation shows good convergence when the covariance parameter $P_0(4,4)$ corresponding to the capacity estimation is 0.5, 1, 5, or 10. It justifies that the proposed fourth EKF method has sufficient robustness for an easy implementation in practical applications.

4.1. Results discussion

4.1.1. Capacity results after different cycles

The battery capacity estimates at the different aging levels of the battery are shown in Fig. 13. The estimates with red (in the web version) cross markers are the average of those t with square and triangle markers. It is clear that capacity fade is predicted with acceptable accuracy. SOH defined by Eq. (6), is also shown in Fig. 13.

$$\mathrm{SOH} = \frac{C_{\mathrm{cap}}}{C_{\mathrm{Nominal}}} \times 100\% \tag{9}$$

where C_{cap} is the actual capacity shown in Fig. 1 and C_{Nominal} is the nominal capacity shown in Table 2.

4.1.2. Resistance results after different cycles

Fig. 14 shows the resistance estimates by the fourth EKF at the different battery ages, with the acceptable accuracy comparing to the ohmic resistance values obtained according to Eq. (3).

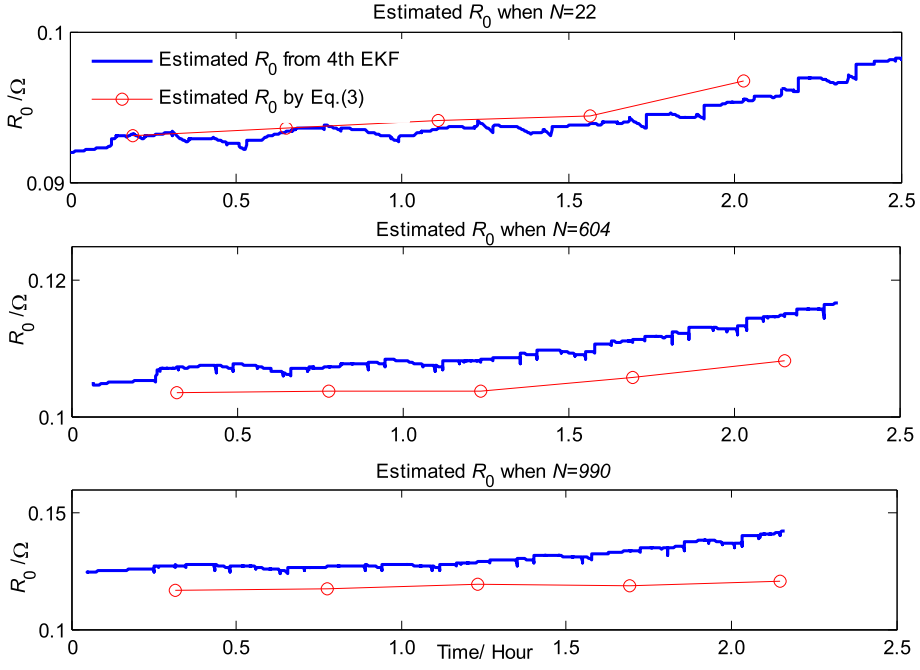

Fig. 14. Resistance estimates during the hybrid pulse test in the different cycles at 22 °C.

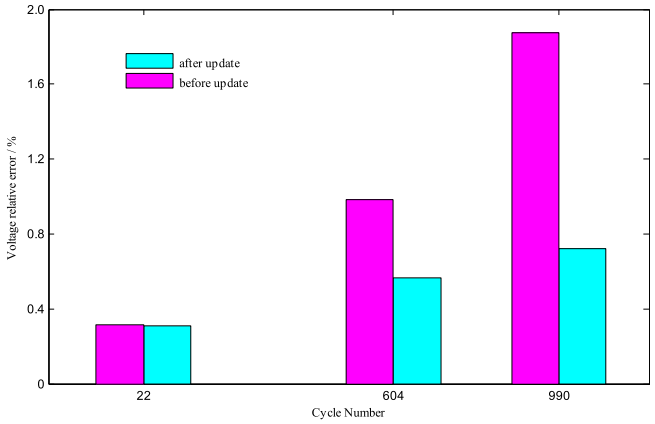

Fig. 15. Voltage errors before and after model recalibration.

4.1.3. Voltage behavior examination

The estimation accuracy for the battery terminal voltage is much improved when the model parameters are updated by means of the fourth-order EKF, especially when the aging of the battery is significant (see Fig. 15). It can be seen that the voltage errors stay below 0.7% after updating parameters.

4.1.4. SOC estimation results

SOC estimation results at different aging levels in the hybrid pulse test are shown in Figs. 16–18. Compared to the second-order EKF without parameters update, the offline fourth-order EKF enhances the accuracy of SOC estimation considerably when the battery ages significantly. It could be concluded that it is undesirable to estimate the battery SOC without considering the capacity and resistance recalibration over the entire battery lifecycle. Since the fourth-order joint EKF is very computationally heavy and may be subject to stability issues, the SOH estimator in this paper is intentionally operated offline, and the related capacity/resistance updates are instead used in the online second-order SOC estimator, resulting in nearly the same SOC trajectory as that in the offline fourth-order one.

5. Further discussion

The fourth-order EKF SOH estimator is regularly used (e.g., after a few hundreds of cycles) when SOC estimation and modeling errors become unacceptable. SOH is manifested as capacity fading and internal resistance increment which extremely slowly alter in practice. Thus, unlike the SOC EKF, we did not set the joint fourth-order EKF online. Offline SOH estimation alleviates the requirement for the algorithm stability (i.e., we can use sufficient batch of data to slowly converge to accurate SOH estimates, see Figs. 11 and 12). Furthermore, as the classic book [39] indicates, this joint fourth-order EKF is an adaptive structure, which may be subject to stability problem. Theoretically, it is still very difficult to derive a proof of stability for this type of estimator. However, Ref. [39] also demonstrates that if model parameters are slowly varying adequately, joint EKF is stable in most cases. In our estimation scenario, the SOH parameters (i.e., capacity and internal resistance) fulfill this slowly-varying requirement very well, which has a marginal adverse influence on the EKF stability, leading to a convergent estimator. Please notice that the joint estimator is offline, instead of real-time realization such that large amounts of data can be exploited to assure its asymptotical convergence. After updating the battery SOH (the model parameters) offline, the online SOC EKF are provided with constant model parameters updated, and thus the single SOC EKF is decoupled with the fourth-order SOH EKF. This is essentially different from two online joint EKFs. Given constant parameters, the SOC EKF often can practically meet stability and convergence requirements.

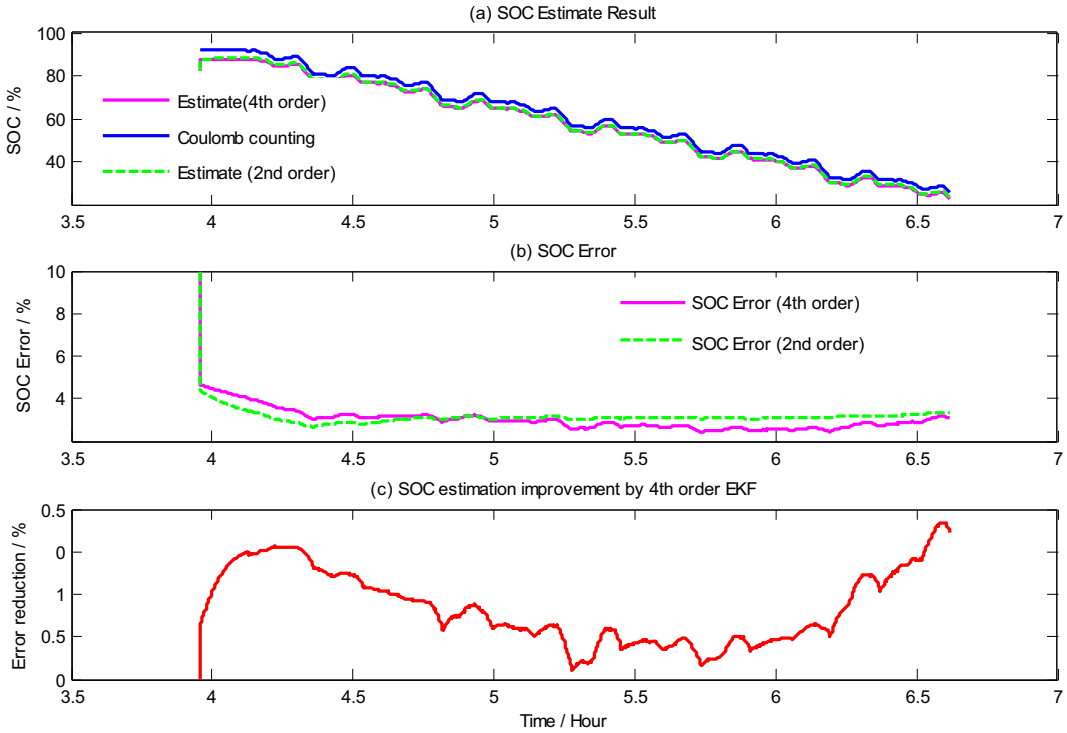

Fig. 16. SOC estimation result for the fresh battery in hybrid pulse test (N = 22, 22 °C).

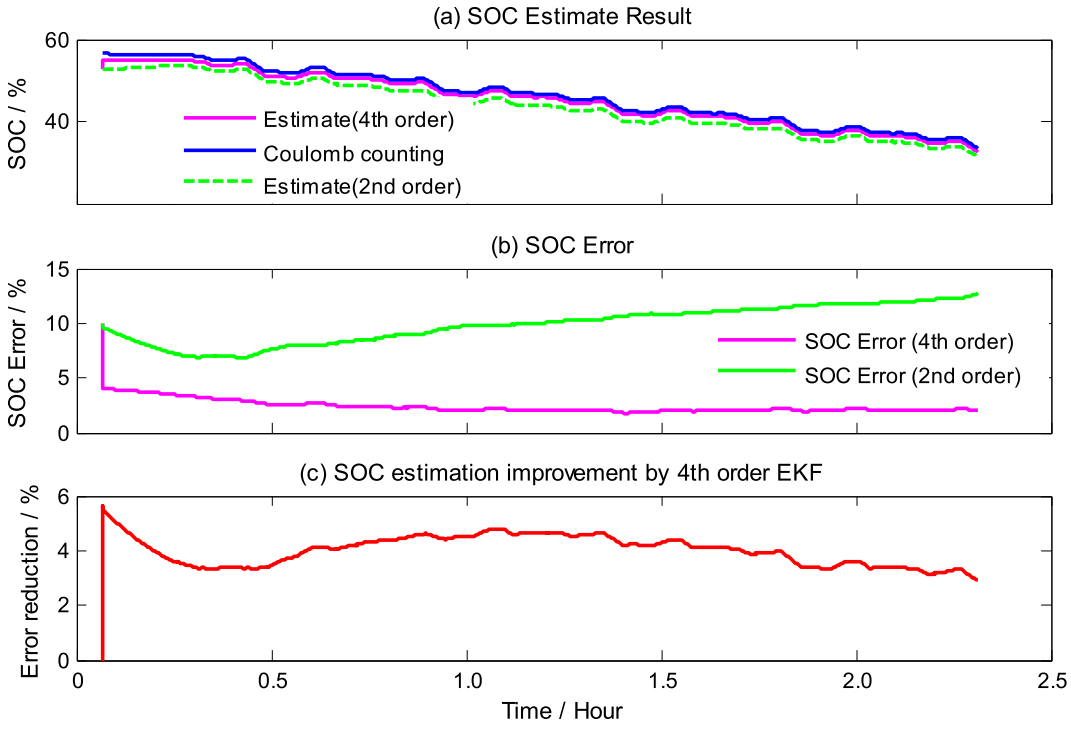

Fig. 17. SOC estimation result for the moderately aged battery in hybrid pulse test ($N = 604$, 22 °C).

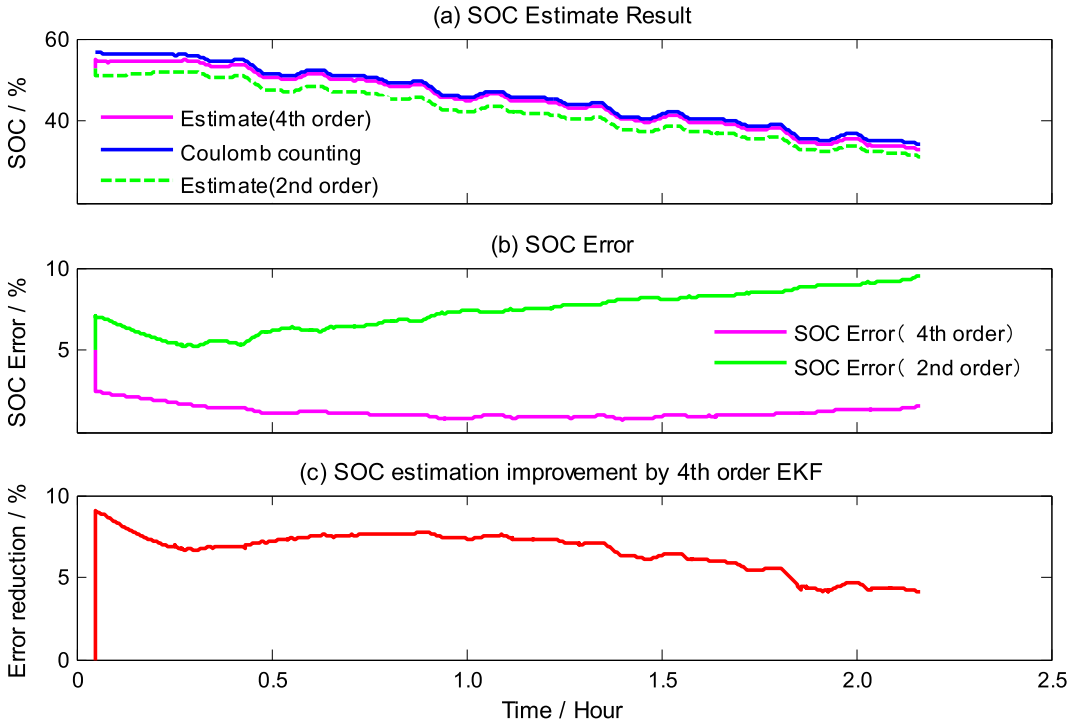

Fig. 18. SOC estimation result for the heavily aged battery in hybrid pulse test ($N = 990$, 22 °C).

6. Conclusions

Recursive least squares algorithm is first employed to identify parameters of the first-order RC model for a LiNMC battery over its cycle lifespan in this article. Then, the performance decay of the nominal model is quantified for different battery aging levels. Based on the modeling results, a multi-scale observer approach is proposed to implement combined SOC/SOH estimation over the lifespan of the lithium-ion battery. The SOC is estimated in real-time by using a second-order EKF, and the SOH (the capacity

and internal ohmic resistance) is updated offline in a fourth-order EKF. The trigger time of the SOH estimator is carefully specified based on the quantified model accuracy deterioration with increasing battery aging. Extensive experimental data are applied to demonstrate that the developed battery monitoring algorithm can provide very accurate SOC and SOH estimates without heavy computational burden and occurrence of instability/divergence.

Acknowledgments

The authors would like to thank Prof. Huei Peng with University of Michigan for sharing the battery experiment data and his valuable suggestions. The scrupulous reviewers are also much appreciated for their helpful comments. The work is supported by National Natural Science Foundation of China (Grant 51375044 and Grant 50905015) and University Talent Introduction Program of China (Grant B12022).

References

[1] S. Piller, H. Smimite, A. Jossen, J. Power Sources 96 (2001) 113–120.
[2] J. Alzieu, H. Sminite, C. Glaize, J. Power Sources 67 (1997) 157–161.
[3] K.S. Ng, C.-S. Moo, Y.-P. Chen, Y.-C. Hsieh, Appl. Energy 86 (2009) 1506–1511.
[4] Data Sheet: Li-ion and Li-pol Battery Gas Gause IC for Portable Applications (bjJUNIOR), Texas Instruments (TI), Dallas, TX, 2007.
[5] L. Lu, X. Han, J. Li, J. Hua, M. Ouyang, J. Power Sources 226 (2013) 272–288.
[6] T. Parthiban, R. Ravi, N. Kalaiselvi, Electrochem. Acta 53 (4) (2007) 1877–1882.
[7] A.J. Salkind, C. Fennie, P. Singh, T. Atwater, D.E. Reisner, J. Power Sources 80 (1999) 293–300.
[8] T. Hansen, C.-J. Wang, J. Power Sources 141 (2005) 351–358.
[9] G.L. Plett, J. Power Sources 134 (2004) 252–261.
[10] G.L. Plett, J. Power Sources 134 (2004) 262–276.
[11] G.L. Plett, J. Power Sources 134 (2004) 277–292.
[12] G.L. Plett, J. Power Sources 161 (2006) 1369–1384.
[13] J. Li, J.K. Barillas, C. Guenther, J. Power Sources 230 (2013) 244–250.
[14] F. Sun, X. Hu, Y. Zou, S. Li, Energy 36 (5) (2011) 3531–3540.
[15] M. Charkhgard, M. Farrokhi, IEEE Trans. Ind. Electron. 57 (2010) 4178–4187.
[16] S. Sepasi, R. Ghorbani, B.Y. Liaw, J. Power Sources 245 (2014) 337–344.
[17] J.P. Wang, Q. Chen, B. Gang, Energy Convers. Manag. 47 (2006) 858–864.
[18] C. Antaloae, J. marco, F. Assadian, IEEE Trans. Veh. Technol. 61 (9) (2012) 3881–3892.
[19] I.-S. Kim, J. Power Sources 163 (2006) 584–590.
[20] I.-S. Kim, IEEE Trans. Power Electron. 4 (25) (2010) 1013–1022.
[21] P.A. Ioannou, J. Sun, Robust Adaptive Control [M], Prentice Hall, Upper Saddle River, 1996.
[22] F. Huer, J. Power Sources 70 (1998) 59–69.
[23] M. Safari, M. Morcrette, A. Teyssot, C. Delacourt, J. Electrochem. Soc. 157 (6) (2010) A145–A153.
[24] P. Ramadass, B. Haran, P.M. Gomadam, R. White, B.N. Popov, J. Electrochem. Soc. 151 (2) (2004) A196–A203.
[25] R. Spotnitz, J. Power Sources 113 (2003) 72–80.
[26] I. Bloom, B.W. Cole, J.J. Sohn, et al., J. Power Sources 101 (2001) 238–247.
[27] T. Matsushima, J. Power Sources 189 (2009) 847–854.
[28] Huolin Li, Jinran Su, Chin. J. Power Sources 32 (4) (2008) 41–45.
[29] S. Lee, J. Kim, J. Lee, B.H. Cho, J. Power Sources 185 (2008) 1367–1373.
[30] P. Singh, C. Fennie, D. Reisner, J. Power Sources 136 (2004) 322–333.
[31] A. Widodo, M.-C. Shim, W. Caesarendra, B.-S. Yang, Expert Syst. Appl. 38 (2011) 11763–11769.
[32] Y.-H. Sun, H.-L. Jou, J.-C. Wu, Energy Convers. Manag. 50 (2009) 2250–2256.
[33] X. Hu, S.E. Li, Z. Jia, B. Egardt, Energy 64 (2014) 953–960.
[34] Hu Chao, D. Byeng, J.C. Younb, Appl. Energy 92 (2012) 694–704.
[35] R. Xiong, F. Sun, Z. Chen, et al., Appl. Energy 113 (2014) 463–476.
[36] X. Hu, S. Li, H. Peng, J. Power Sources 198 (2012) 359–367.
[37] X. Hu, F. Sun, Y. Zou, J. Cent. South Univ. Technol. 18 (2011) 1525–1531.
[38] X. Hu, F. Sun, Y. Zou, H. Peng, in: American Control Conference (ACC), 2011, pp. 935–940.
[39] P.A. Ioannou, J. Sun, Robust Adaptive Control, Courier Dover Publications, 2012.